

Bias Attribution of the Diurnal Variation of Regional Precipitation Events over the Middle and Lower Yangtze River Basin in Summer Predicted by the Shanghai Regional Dynamical Forecast System

Journal:	*Advances in Atmospheric Sciences*
Manuscript ID	AAS-2026-0204.R1
Manuscript Type:	Original Article
Date Submitted by the Author:	04-Aug-2026
Complete List of Authors:	Li, Ziqi; School of Atmospheric Sciences, Nanjing University, School of Atmospheric Sciences, Nanjing University Huang, Anning; School of Atmospheric Sciences, Nanjing University, School of Atmospheric Sciences, Nanjing University Dong, Guangtao ; Shanghai Meteorological Service Gu, Chunlei; School of Atmospheric Sciences, Nanjing University, School of Atmospheric Sciences, Nanjing University Wu, Rongchang; School of Atmospheric Sciences, Nanjing University, School of Atmospheric Sciences, Nanjing University

in press

SCHOLARONE MANUSCRIPTS

Bias Attribution of the Diurnal Variation of Regional Precipitation Events over the Middle and Lower Yangtze River Basin in Summer Predicted by the Shanghai Regional Dynamical Forecast System

Ziqi Li[1,3], Anning Huang[1,4*], Guangtao Dong[2,3], Chunlei Gu[1], Rongchang Wu[1]

1. School of Atmospheric Sciences, Nanjing University, Nanjing 210023, China

2. Shanghai Climate Center, Shanghai Meteorological Service, Shanghai 200030, China

3. Key Laboratory of Cities' Mitigation and Adaptation to Climate Change in Shanghai, China Meteorological Administration, Shanghai 200030, China

4. Qinghai Lake Comprehensive Observation Research Station, Chinese Academy of Sciences, Gangcha 812300, China

Corresponding authors: **Prof.** Anning Huang anhuang@nju.edu.cn;

Prof. Guangtao Dong gtdong@163.com

In Press
For Review Only

Abstract

Using hourly rain gauge observations and ERA5 reanalysis, this study evaluates the performance of the Shanghai Regional Dynamical Forecast System (WRF_CFSv2) at lead times of 13–36 h in forecasting the diurnal variation of summer regional precipitation events (RPEs) over the middle and lower Yangtze River Basin (MLYRB) and investigates the possible causes related to model biases. The results indicate that WRF_CFSv2 can well reproduce the diurnal phase of precipitation amount of RPEs despite the magnitude overestimation throughout the day. The observed occurrence of RPEs and corresponding atmospheric circulation can also be reasonably captured. However, the WRF_CFSv2 exhibits a systematic overestimation of the intensity, occurrence, and spatial coverage of RPEs. Further analysis attributes these biases primarily to the overestimation of dynamic factors, with thermal factors playing a secondary role. Dynamically, the WRF_CFSv2 produces a persistent anomalous low-level cyclone over the MLYRB which leads to the overestimation of the low-level southwesterly winds and water vapour flux convergence (WVFC), acting as the dominant driver for the overestimated nocturnal RPEs. Thermally, a warm bias in the predicted daytime surface conditions leads to a more unstable lower troposphere and strengthened convective available potential energy (CAPE). Rather than acting independently, this overestimated daytime instability combines with strong WVFC and evaporation, functioning as a synergistic factor that culminates in the overestimated daytime RPEs. By evaluating the capability in predicting RPEs and elucidating the

For Review Only
in Press

sources of model biases, this study provides a scientific basis for optimizing and modifying the physical parameterization schemes of WRF_CFSv2 in future.

Key words: the middle and lower Yangtze River basin; diurnal variation of precipitation; summer; regional precipitation events; prediction; bias attribution

https://doi.org/10.1007/s00376-026-6204-4

Article Highlights:

- The WRF_CFSv2 can well capture the spatial distribution of summer precipitation in MLYRB, although it tends to overestimate the magnitude.
- The diurnal cycle pattern of the regional precipitation amount in MLYRB can be well reproduced by the WRF_CFSv2.
- The overestimation of precipitation is mainly attributed to the overestimated atmospheric dynamical factors.

For Review Only

in Press

1. Introduction

The diurnal cycle of precipitation is a fundamental component of the Earth's climate system, primarily driven by solar radiation and influenced by both regional and synoptic-scale dynamic and thermal conditions (Dai et al., 1999; Sorooshian et al., 2002; Dai and Trenberth, 2004). Extensive research has been dedicated to understanding the characteristics, mechanisms, and propagation of the diurnal variation of precipitation (Zhou et al., 2008; Chen et al., 2009; Chen et al., 2013; Guo et al., 2017; Wu et al., 2018; Xue et al., 2018; Zhu et al., 2018; Fu et al., 2019; Zhang et al., 2019). It is generally characterized by a precipitation diurnal peak in the late afternoon over land and in the early morning over the ocean.

The middle and lower Yangtze River Basin (MLYRB) lies within the East Asian monsoon region and constitutes a core area of the Yangtze River Economic Belt, where population and industry are highly concentrated. Its dense urban agglomerations, agricultural production areas, and transportation infrastructure make the region particularly vulnerable to persistent heavy rainfall. Persistent heavy rainfall is a primary cause of secondary meteorological disasters such as summer floods, urban waterlogging, and landslides, posing significant challenges to socioeconomic development (Hu et al., 2019; Tang et al., 2021; Zeng et al., 2023; Wu et al., 2025). The diurnal cycle of summer precipitation in the MLYRB exhibits unique features arising from complex interactions among surface heating, orography, and the monsoon flow (Yu et al., 2007a; Yu et al., 2007b). Specifically, it displays a bimodal phase with one diurnal peak at 08:00 Beijing time (BJT) and the other at 18:00 BJT (Xu et al., 2021;

In Press
For Review Only

72 Wei et al., 2024). The morning peak is predominantly associated with stratiform
73 precipitation, whereas the late afternoon peak is linked to convective precipitation
74 (Chen et al., 2012; Wu et al., 2025). Furthermore, the geographical distribution of the
75 precipitation diurnal variation along the Yangtze River valley exhibits a distinct
76 eastward-propagating phase delay in the timing of the precipitation diurnal peak.
77 Notably, over 60% of the summer precipitation in the MLYRB is contributed by the
78 RPEs characterized by large spatial coverage and long duration (Wu et al., 2025). Given
79 that RPEs are the primary drivers of severe regional flooding and involve complex
80 interactions between synoptic forcing and mesoscale systems, improving the forecast
81 skill of the RPEs is of high priority for disaster prevention and mitigation.

82 The accurate simulation of the diurnal variation of precipitation serves as a critical
83 benchmark for evaluating the performance of numerical weather and climate models
84 (Dai, 2006). The ability of a numerical model to precisely capture the phase and
85 amplitude of the precipitation diurnal cycle presents a stringent test of its internal
86 physical parameterization schemes, including those for convection, planetary boundary
87 layer (PBL) evolution, and land surface processes (Qiao and Liang, 2016; Yang et al.,
88 2018; Zhao et al., 2024). Existing model evaluations suggest that convection-
89 parameterized simulations tend to produce rainfall too frequently, underestimate
90 rainfall intensity, and shift the diurnal peak too early over the lower Yangtze River,
91 whereas convection-permitting simulations improve the phase and duration of
92 precipitation but often remain too wet and may over-amplify early-morning rainfall or
93 eastward-propagating precipitation signals linked to an overly strong nocturnal low-

For Review Only
in Press

level jet (Guo et al., 2020; Li et al., 2020b; Dong et al., 2022).

While previous studies have extensively evaluated these biases, most have relied on single-site or grid-point based assessments. This traditional approach treats precipitation as isolated occurrences in space, neglecting the spatiotemporal evolution of precipitation systems (Guo et al., 2017; Hu and Yuan, 2021). Actual precipitation systems, especially RPEs, possess specific life cycles, moving trajectories, and spatial extents. Therefore, to effectively diagnose the key physical deficiencies in models, it is imperative to shift from single-point statistics to an RPE evaluation focused on the entire lifecycle of precipitation events.

To address these limitations and deepen the understanding of model behaviors, this study utilizes high-resolution observational data and the forecast results of WRF_CFSv2 to systematically investigate the ability of WRF_CFSv2 in predicting the diurnal variation of RPEs over the MLYRB in summer and possible causes related to the model biases. This study aims to address the following questions: (1) How is the ability of the WRF_CFSv2 in predicting the diurnal variation of RPEs in summer over the MLYRB? (2) What are the main sources of the model errors?

The remainder of this study is organized as follows: Section 2 describes the data sets and methods used in this study. In Section 3, the performance of WRF_CFSv2 in predicting the diurnal cycle of RPEs over the MLYRB in summer and possible causes related to model biases are addressed. The summary and discussion are provided in Section 4.

For Review Only
in Press

2. Data and Methods

2.1 Data

The datasets used in this study are described below:

The study area and rain gauge data: The MLYRB is defined as the region within 28°–33°N and 110°–123°E. The hourly observed rain gauge precipitation data from 1329 stations over the MLYRB (Fig. 1b) in the summers (June–August) of 2020 to 2024 are provided by the China Meteorological Administration (CMA), which have been quality controlled by National Meteorological Information Center of CMA (Zhang et al., 2016).

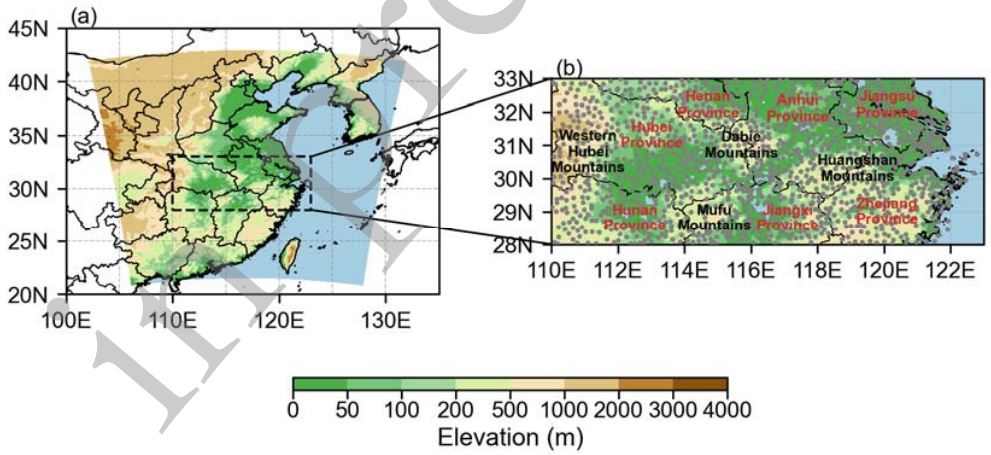


Fig. 1. (a) Spatial distribution of terrain height over the simulation region in the WRF_CFSv2. The area enclosed by the dashed line is the MLYRB region (b, 28°–33°N, 110°–123°E) studied in this paper.

This study utilized the ERA5 reanalysis dataset from the European Centre for Medium-Range Weather Forecasts (ECMWF) (Hersbach et al., 2020), which has a

For Review Only

temporal resolution of one hour, spatial resolution of 0.25° × 0.25° at 37 pressure levels. Pressure-level variables used in this study include the u- and v-components of wind, geopotential height, air temperature, vertical velocity, and specific humidity. Single-level variables include total column water vapour, evaporation, total precipitation, and CAPE. In addition, the 2m air temperature, surface latent and sensible heat fluxes data from the ERA5 Land reanalysis dataset with a spatial resolution of 0.1° × 0.1° and temporal resolution of 1 hour are also used in this study.

The global terrain data used in this study is derived from the 2025 General Bathymetric Chart of the Oceans (GEBCO_2025). This dataset provides global coverage of land elevation and ocean bathymetry data in meters (m) with a horizontal spatial resolution of 15 arc-seconds (GEBCO Bathymetric Compilation Group 2025, 2025).

The forecast data used in this study were generated by the Shanghai Regional Dynamical Forecast System (WRF_CFSv2). Initiated in 2013 and developed by the Shanghai Climate Center based on the WRF-ARW model version 3.9.1 (Skamarock et al., 2008), the system has been operational since July 2016. The operational WRF_CFSv2 is a single-member deterministic forecasting system capable of producing forecasts with lead times of up to 60 days. However, the archived 60-day operational products do not contain the continuous hourly model output required to analyze the precipitation diurnal cycle. Therefore, this study uses a dedicated set of retrospective forecasts for the summers of 2020–2024. The retrospective forecasts were produced on the native 9-km WRF_CFSv2 grid. The model domain covers Eastern

For Review Only
in Press

China (Fig. 1a) with 265 × 265 horizontal grid points and 38 vertical levels. The physical parameterization schemes used include the WSM3 microphysics scheme (Hong et al., 2004), the Yonsei University (YSU) planetary boundary layer scheme (Hong et al., 2006), the Noah land surface model (Chen and Dudhia, 2001), the RRTMG schemes for short- and long-wave radiation (Iacono et al., 2008), and the Grell-Freitas (GF) cumulus parameterization scheme (Grell and Freitas, 2014). The initial and lateral boundary conditions for the WRF_CFSv2 were derived from the 6-hourly NCEP Climate Forecast System Version 2 (CFSv2) forecasts at a horizontal resolution of 0.5° × 0.5° (Saha et al., 2014). The retrospective forecast initialized at 00:00 UTC of each day in summer was run with a rolling forecast of future 36 hours. Following Cai et al. (2021), to avoid the impact of the initial spin-up period, we utilized the results during the forecast period of 13-36 h for analysis.

2.2 Methods

In this study, a threshold of 0.1 mm h^{-1} is applied to define valid precipitation for each hour. Following Zhou et al. (2008) and Wu et al. (2018), the climatic mean precipitation amount is calculated as the accumulated valid precipitation divided by the total hours during the summers of 2020–2024, the climatic mean precipitation frequency is the percentage of the total precipitating hours to the total hours of the 5 summers, and the climatic mean precipitation intensity equals the climatic mean precipitation amount divided by the climatic mean precipitation frequency. We use Beijing time (BJT) to reveal the diurnal variation of precipitation characteristics and large-scale atmospheric circulation in our analysis.

In Press
For Review Only

In this study, to directly evaluate the model's performance at station locations while avoiding spatial smoothing, we used the nearest neighbor method to match the model grid point values to station coordinates for analyzing the precipitation. Atmospheric circulation and moisture variables on pressure levels were bilinearly interpolated onto the 0.25° × 0.25° ERA5 grid, whereas near-surface variables, including 2-m air temperature and surface sensible and latent heat fluxes, were bilinearly interpolated onto the corresponding 0.1° × 0.1° ERA5-Land grid.

An RPE is defined as the persistent occurrence of widespread precipitation within a given region (Li et al., 2020a; Hu and Yuan, 2021). For observational data, we first created a time series of the number of stations with simultaneous precipitation (≥0.1 mm h^{-1}) for each hour during the summers of 2020–2024. Following the approach of Guo et al. (2017), an hour is classified as an RPE hour if the precipitation spatial coverage equals or exceeds 20% of the total number of stations in the MLYRB. No additional minimum-duration criterion is imposed: consecutive RPE hours constitute a single RPE, whereas two RPE periods separated by at least one non-RPE hour are treated as two independent events. An hour that meets the valid-precipitation threshold but has a spatial coverage below 20% is defined as an LPE hour. Table 1 summarizes the differences between RPEs and LPEs.

Table 1. Definitions of regional precipitation events (RPEs) and local precipitation events (LPEs)

In Press
For Review Only

Event type	Valid-precipitation threshold	Spatial-coverage criterion	Temporal criterion and event separation
RPE	Hourly station precipitation ≥ 0.1 mm h^{-1}	Percentage of stations with valid precipitation ≥ 20%	Consecutive RPE hours constitute a single event. Two RPE periods separated by at least one non-RPE hour are treated as two events. No minimum duration is imposed.
LPE	Hourly station precipitation ≥ 0.1 mm h^{-1}	0% <Percentage of stations with valid precipitation < 20%	A valid-precipitation hour that does not meet the spatial-coverage criterion for an RPE.

Based on this criterion, we detected 2299 RPE occurrence hours in the summers of 2020-2024. An individual RPE is defined by a period of continuous RPE hours, a total of 122 RPEs are obtained. For evaluating the WRF_CFSv2's ability to reproduce the diurnal characteristics of observed RPEs, the analysis of precipitation amount, intensity, and spatial coverage rate (the ratio of the number of stations with valid precipitation to the total number of stations in the MLYRB during the RPEs) of the RPEs focuses on the time periods corresponding to these observed 122 RPEs.

Following Wu et al. (2025), for each RPE hour, we define the number of stations with valid precipitation as N, while the total number of observed stations is 1329, and the rainfall at the i station among the N precipitation stations as r_i. The regionally mean precipitation amount, intensity and the spatial coverage rate at each RPE hour can be given by:

$$\text{Precipitation amount} = \frac{\sum_{i=1}^{N} r_i}{1329} \quad (1)$$

in Press
For Review Only

$$\text{Precipitation intensity} = \frac{\sum_{i=1}^{N} r_i}{N} \tag{2}$$

$$\text{Coverage rate} = \frac{N}{1329} \times 100\% \tag{3}$$

Using these equations, time series for precipitation amount, intensity, and coverage rate are obtained for each RPE hour. To evaluate the WRF_CFSv2's forecasting skill, we identified predicted RPE hours using the same observational threshold (coverage rate $\geqslant$ 20%). The hit rate is defined as the number of hours identified as RPE hours by both the WRF_CFSv2 and the observations divided by the total number of observed RPE hours. The diurnal cycle of the hit rate is calculated by separately tallying the numerator and denominator for each BJT hour.

Extensive research has utilized cluster analysis to classify the diurnal cycle of precipitation and to assess model performance in reproducing observed patterns (Vigaud et al., 2018; Wu et al., 2018; Zhu et al., 2018; Robertson et al., 2020; Liu et al., 2021; Lai et al., 2025). We follow the methodology of Vigaud et al. (2018), Robertson et al. (2020), and Liu et al. (2021). The multi-year mean hourly precipitation of RPEs during summer, which represents the diurnal cycle, is organized into a 24-dimensional vector for each grid point. This vector is then normalized using the formula:

$$D_a(h) = \left[\frac{R_a(h)}{\frac{1}{24}\sum_{i=1}^{24} R_a(i)} - 1 \right] \tag{4}$$

Where $D_a(h)$ is the normalized precipitation of RPEs at hour h and $R_a(h)$ is the

In Press
For Review Only

original precipitation of RPEs at hour h. The K-means algorithm is then applied to these normalized vectors to identify the dominant spatial patterns of the diurnal cycle. Finally, the normalized 24-dimensional vectors from the model simulation are projected onto the diurnal patterns of the K-means regimes derived from the observation data. Each model-simulated station point is then assigned to the closest regime based on the smallest Euclidean distance.

We perform a moisture budget analysis following previous studies (Seager et al., 2010; Chou and Lan, 2012; Li, 2018; Li et al., 2020b; Chen et al., 2025). The moisture budget equation is given by under the p coordinate system:

$$P = \left\langle \frac{\partial q}{\partial t} \right\rangle + \left\langle \nabla_h \cdot (q\vec{V}_h) \right\rangle + \left\langle \frac{\partial(\omega q)}{\partial p} \right\rangle + E + \delta \tag{5}$$

Let < > equal to the $-\frac{1}{g}\int_{P_s}^{P_t} dp$, P_s and P_t represent the surface and top layer pressure, respectively. P and E denote precipitation and evaporation, $\langle \frac{\partial q}{\partial t} \rangle$ signifies the changes in local water vapour with time, $\langle \nabla_h \cdot (q\vec{V}_h) \rangle$ is the horizontal WVFC (where $\nabla_h = \frac{\partial}{\partial x} + \frac{\partial}{\partial y}$), and $\langle \frac{\partial(\omega q)}{\partial p} \rangle$ describes the water vapour flux in vertical transport. Each term on the right side of Eq. (5) during the RPEs is calculated by using the hourly WRF_CFSv2 predictions and ERA5 reanalysis data.

To reveal the relationship between the spatial distribution of the variables (wind and sensible heat flux) and sub-grid terrain fluctuations, this study introduces the sub-grid topography standard deviation (STD) to quantify local terrain variations. Since the target variables, wind and sensible heat flux, have spatial resolutions of 0.25° and 0.1°

For Review Only
in Press

respectively, the 15 arc-second resolution GEBCO_2025 elevation data (GEBCO Bathymetric Compilation Group 2025, 2025) must be mapped onto these two target grids for calculation. For any given target grid (i, j), the sub-grid topography standard deviation $STD_{i,j}$ is calculated as follows:

$$STD_{i,j} = \sqrt{\frac{1}{N}\sum_{i_1=1}^{n}\sum_{j_1=1}^{n}\left[h(i_1, j_1) - \overline{h}_{i,j}\right]^2} \quad (6)$$

Where $h(i_1, j_1)$ represents the elevation value of the GEBCO_2025 data at the west-east index i_1 and south-north index j_1 within the target grid (i, j). $\overline{h}_{i,j}$ is the regional mean terrain elevation within that specific target grid. *N* is the total number of original GEBCO_2025 elevation data points contained within the target grid ($N = n \times n$). For the sensible heat flux data on the 0.1° ERA5-Land grid and the 850-hPa wind data on the 0.25° ERA5 grid, *n* is set to 24 and 60, respectively.

3. Results

3.1 Characteristics of Total and RPE Rainfall over the MLYRB in Summer

Figure 2 shows the summer mean precipitation amount, frequency, and intensity for the total rainfall over the MLYRB from the observations and the WRF_CFSv2 outputs. The observed precipitation amount exhibits a pattern with higher values in the east and lower values in the west (Fig. 2a) with high-value centers located in the Huangshan Mountains (near 118°E, 29.5°N), Dabie Mountains (near 116°E, 31°N), the mountainous region of Hunan and Hubei (near 110°E, 33°N), and the coastal area of Zhejiang Province (near 121°E, 29.5°N). The WRF_CFSv2 successfully captures this

In Press
For Review Only

overall spatial pattern (Fig. 2b) with a spatial correlation coefficient of 0.68 between the WRF_CFSv2 predictions and observations, indicating that the WRF_CFSv2 can reasonably reproduce the locations of the main precipitation centers. However, the WRF_CFSv2 tends to overestimate the summer precipitation amount over most of the MLYRB, especially over the mountainous areas.

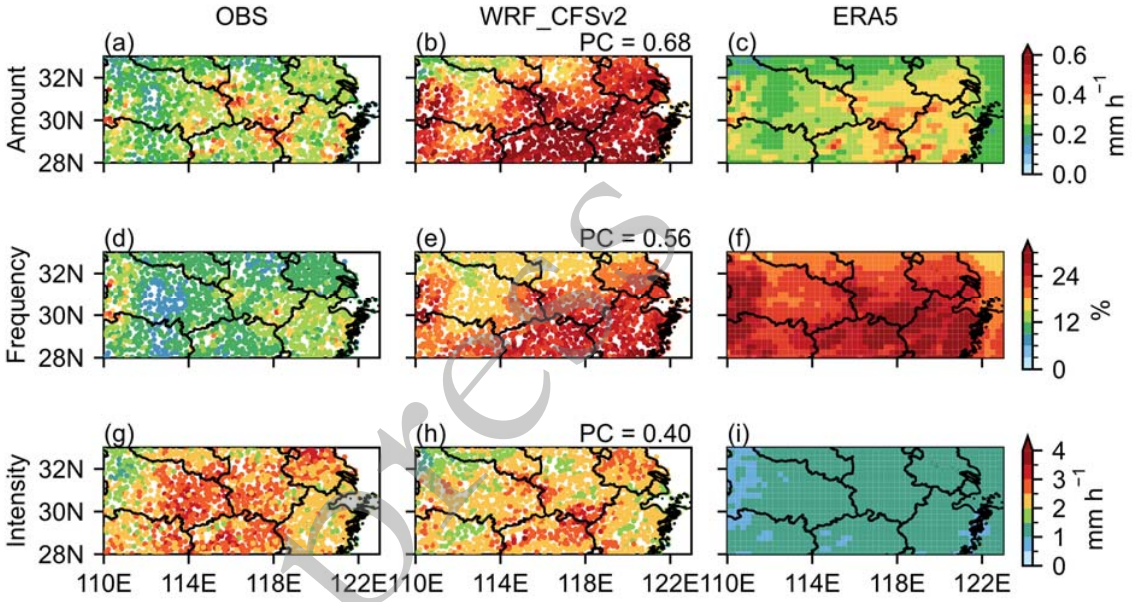


Fig. 2. The spatial distribution of the summer mean precipitation amount, frequency, and intensity averaged over 2020-2024 from the observation, WRF_CFSv2 prediction and ERA5 reanalysis.

The observed summer mean precipitation frequency shows a large-scale pattern similar to precipitation amount (Figs. 2a, d). In the Huangshan Mountains, Dabie Mountains, Zhejiang Province, and western Hubei mountainous areas, the precipitation frequency is about 15%, while it is about 10% in the other areas. The WRF_CFSv2 can reproduce the spatial distribution of precipitation frequency to some extent (spatial

In Press Only

correlation coefficient of 0.56) but exhibits a systematic overestimation (Fig. 2e).

The observed precipitation intensity is relatively higher in the central MLYRB and southern Jiangsu province compared to the other regions (Fig. 2g). The WRF_CFSv2 can well produce a similar magnitude of precipitation intensity, but it shows relatively lower skill for producing the spatial pattern of precipitation intensity (spatial correlation coefficient of 0.40) (Fig. 2h) relative to the precipitation amount (Fig. 2b) and frequency (Fig. 2e). ERA5 reproduces the observed magnitude and spatial distribution of precipitation amount reasonably well (Fig. 2c) but overestimates precipitation frequency and underestimates precipitation intensity (Figs. 2f, i).

Accounting for the majority of total summer precipitation, the climatic mean rainfall of RPEs exceeds 200 mm across most of the MLYRB (Fig. 3b). Its spatial distribution closely mirrors that of RPE hours (Fig. 3k). In comparison with the observations, the WRF_CFSv2 generally reproduces the spatial distribution of both the total and RPE rainfall (Figs. 3a, b, d and e), albeit with a noticeable wet bias (Figs. 3g, h). Specifically, the total rainfall is significantly overestimated in the southeast (Fig. 3g), while the centers of positive bias for RPE exhibit a southwest-northeast orientation (Fig. 3h). Regarding the RPE hours, the WRF_CFSv2 exhibits a widespread overestimation across the MLYRB, which is particularly pronounced in the south (Fig. 3q). In contrast, both the precipitation amount and rainy hours of the predicted local precipitation events (LPEs) are comparable to the observations (Figs. 3c, f, l and o). Meanwhile, the biases of predicted LPEs (Figs. 3i, r) are much lower relative to the RPEs (Figs. 3h, q), indicating that the biases of the predicted total rainfall (Figs. 3g, p)

For Review Only
in Press

are mainly contributed by those of the predicted RPEs.



Fig. 3. Spatial distributions of summer-mean accumulated precipitation (a–i; unit: mm) and precipitation hours (j–r; unit: h) for total precipitation, RPEs, and LPEs, averaged over the summers of 2020–2024. The columns from left to right represent total precipitation, RPEs, and LPEs, respectively. Observations are shown in (a–c) and (j–l), WRF_CFSv2 predictions are shown in (d–f) and (m–o), and the corresponding differences are shown in (g–i) and (p–r). All differences are calculated as WRF_CFSv2 predictions minus observations.

3.2 Diurnal Cycle of RPEs

As demonstrated in the previous section, the RPEs dominate both the occurrence

in press only

and amount of summer rainfall in the MLYRB, and that the precipitation bias predicted by the WRF_CFSv2 is primarily dominated by the RPEs. Consequently, this study prioritizes the analysis of RPEs. However, due to the inherent 'drizzle bias' in the model, the WRF_CFSv2 significantly identifies more RPE instances than are observed. Therefore, to evaluate the WRF_CFSv2's capability in forecasting events of real-world significance, this study specifically assesses the performance of WRF_CFSv2 during the observed RPEs.

To investigate the characteristics of the diurnal precipitation cycle of RPEs, we employed K-Means clustering to classify the diurnal variations of regional precipitation into three distinct types, as illustrated in Figure 4. From the observations (Figs. 4a, c), the first type (blue) exhibits a bimodal structure with a primary peak in the afternoon, located primarily in western Hubei Province and southeastern Zhejiang Province. The second type (red) is characterized by daytime-dominant precipitation and higher precipitation amounts, mainly distributed across complex terrain regions such as the Huangshan, Dabie, and Mufu Mountains. The third type (orange) displays a bimodal pattern featuring a primary early-morning peak; this type surrounds the second type in a southwest-northeast orientation. From the predictions (Figs. 4b, d), the spatial distribution of the diurnal cycle of regional precipitation predicted by the WRF_CFSv2 is generally consistent with the observations. However, the predicted distributions for the second and third types exhibit a southeastward shift. This displacement is consistent with the southern bias of the predicted RPEs presented in Figures 3n and q. Furthermore, the WRF_CFSv2 overestimates the precipitation amounts across all types. It also

For Review Only
in Press

exaggerates the afternoon precipitation peaks for the second and third types, while shifting their early-morning peaks one hour earlier.

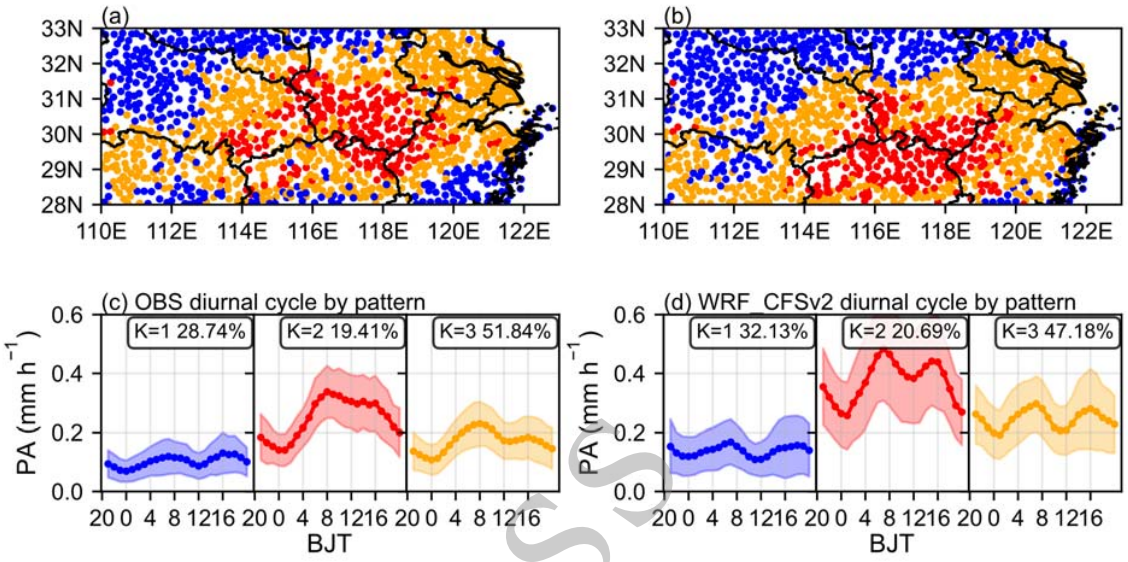


Fig. 4. Spatial distribution of precipitation amount patterns for the RPEs and corresponding diurnal cycles in the MLYRB averaged over the summers of 2020-2024 from the observations (a, c) and predictions (b, d). Different colors represent different types of diurnal cycles. The curves in **c** and **d** represent the precipitation amount of RPEs regionally averaged over the stations belonging to a given type. The markers of patterns K in **a** (**b**) are labeled at **c** (**d**), accompanied by the ratio of the stations belonging to a given type to the total stations in the MLYRB. Shadings in **c** and **d** show the standard deviation of the precipitation amount among the stations belonging to a given type.

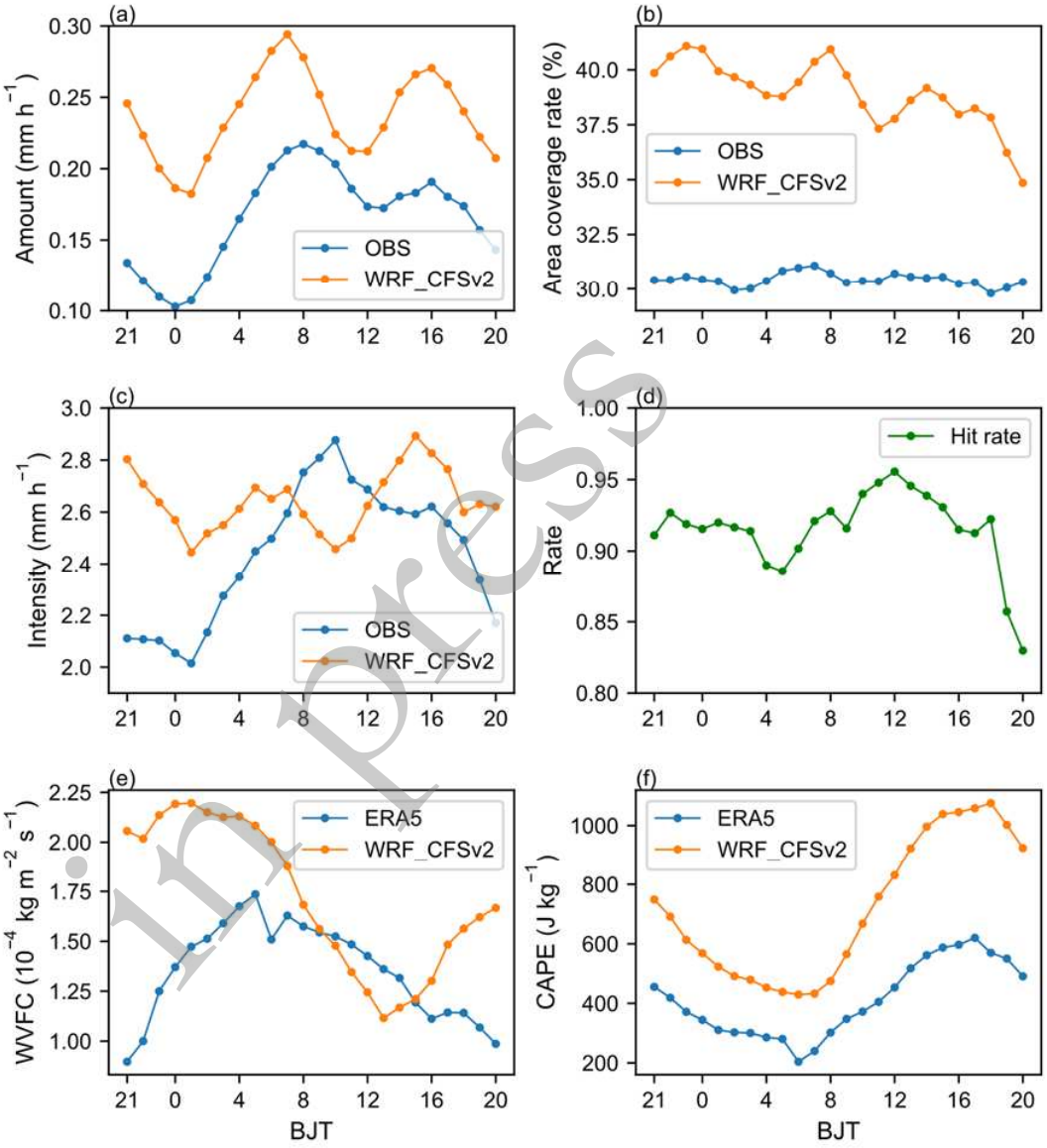
As shown in Figure 5a, the WRF_CFSv2 can reasonably reproduce the diurnal cycle phase of the regional precipitation amount with bimodal structure featured by one dominant morning peak and a secondary afternoon peak, but it overestimates the

In Press
Review Only

precipitation amount throughout a day and the predicted morning peak is one hour earlier than the observation. In addition, the WRF_CFSv2 generally overestimates the coverage rate of RPEs throughout a day with the magnitudes ranging from ~5% to ~10% (Fig. 5b). The observed intensity of RPEs shows two diurnal peaks with one at 10:00 BJT and the other at 16:00 BJT. The WRF_CFSv2 can produce two diurnal precipitation intensity peaks of RPEs, but the predicted peaking time is 1-3 hours earlier than the observation and the precipitation intensity of RPEs at most hours of a day is overestimated (Fig. 5c). Overall, both the overestimated coverage rate and precipitation intensity contribute to the overestimation of the rainfall amount of the RPEs. Furthermore, the hit rate of the RPEs remains more than 85% at almost all hours of a day, indicating that the WRF_CFSv2 can well capture the observed RPEs (Fig. 5d). The model's performance in simulating these precipitation characteristics is closely tied to its representation of moisture supply and thermodynamic instability. Regarding moisture supply, the diurnal peak of column-integrated (from surface to 100 hPa) WVFC of ERA5 occurs at 05:00 BJT (Fig. 5e), while the WRF_CFSv2 generally reproduces this diurnal cycle, a distinct phase shift is evident: the predicted peak occurs at 01:00 BJT, four hours earlier than in ERA5. This four-hour phase lead aligns closely with the phase lead of the morning precipitation peak predicted by the WRF_CFSv2. In terms of thermodynamic instability (Fig. 5f), the CAPE in both WRF_CFSv2 and ERA5 reaches its daily maximum around 18:00 BJT, indicating that the WRF_CFSv2 can also reasonably capture the diurnal variation of atmospheric instability. Ultimately, the WRF_CFSv2's ability to broadly reproduce the diurnal characteristics of both

In Press
For Review Only

372 WVFC and CAPE explains why the WRF_CFSv2 can successfully reproduce the
373 observed diurnal phase of RPEs. The discontinuity around 20:00–21:00 BJT coincides
374 with the transition from the 36-h forecast of one cycle to the 13-h forecast of the next.



375

376 **Fig. 5.** Diurnal variation of precipitation amount (a), area coverage rate (b),
377 precipitation intensity (c) of the RPEs in the MLYRB from the observations and
378 predictions averaged over summers of 2020-2024, and the hit rates of WRF_CFSv2 for
379 RPEs (d). The diurnal variations of the vertically integrated (surface to 100hPa) WVFC

In press

(e) and CAPE (f) during the RPEs regionally averaged over the MLYRB in the summers of 2020-2024.

3.3 Possible Causes Related to the Prediction Biases of RPEs

Possible causes related to the atmospheric circulation biases that lead to the errors in the predicted rainfall over the MLYRB during the observed RPEs are discussed in the following sections. As pointed out by previous studies (Xue et al., 2018; Fu et al., 2019), the morning precipitation peak in the central eastern China during the typical Meiyu season is related to the nocturnal acceleration of the southwesterly flow, which may be due to the inertial oscillations in the boundary layer, i.e., the weakening of turbulent friction after sunset leads to an imbalance between the Coriolis force and the pressure gradient force.

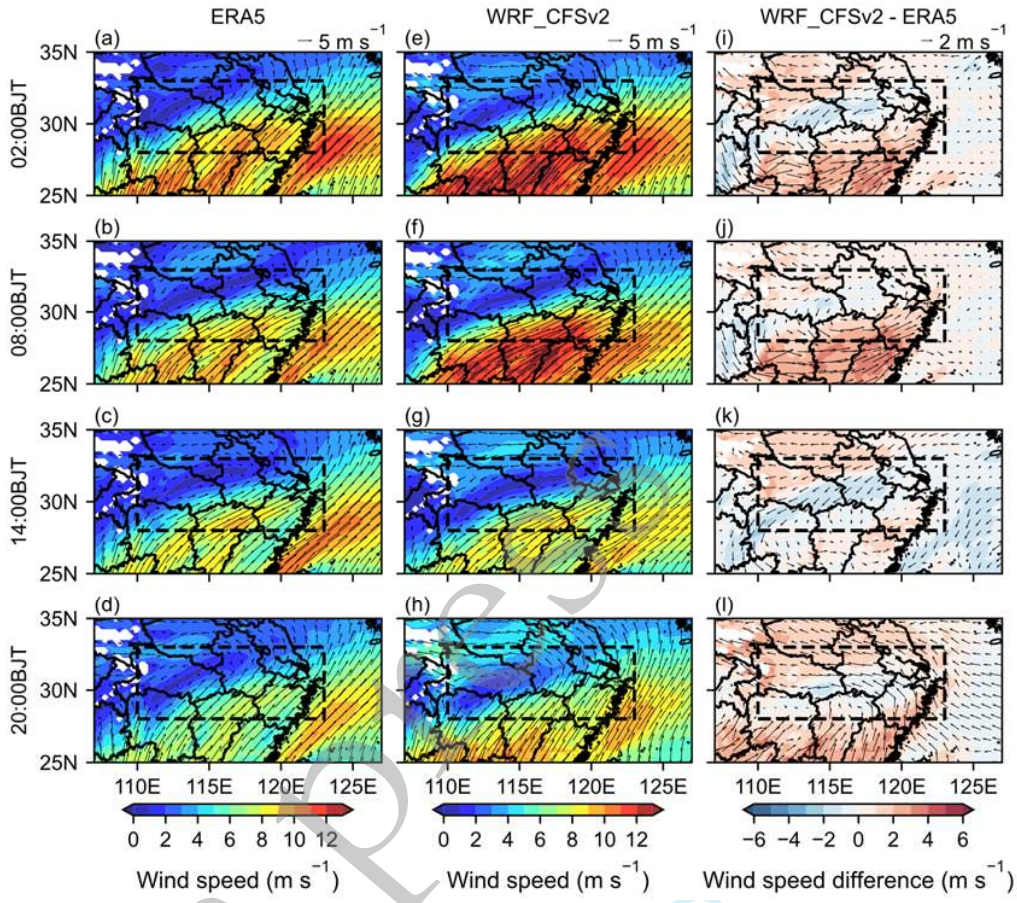
As shown in Figure 6, the 850 hPa winds of ERA5 over the regions south of 30°N are stronger at night and weaker in the afternoon. The WRF_CFSv2 reproduces this characteristic well but overestimates the wind speed almost throughout the day, which likely contributes to the overestimation of precipitation by enhancing water vapour transport. Further analysis of the anomalous wind field reveals that the MLYRB is dominated by an anomalous cyclonic circulation throughout most of the diurnal cycle, which is associated with the overestimation of WVFC (Figs. 9g, h). Notably, the anomalous cyclonic circulation exhibits significant strengthening and enhanced organization at night, suggesting that the nocturnal precipitation overestimation is associated with more favorable dynamical conditions compared to the daytime.

For Review Only
in Press

Furthermore, the overestimation of nocturnal and early-morning 850 hPa wind speeds intensifies with sub-grid terrain complexity (Fig. 8e), indicating the importance of improving the representation of sub-grid topographic dynamical effects, such as sub-grid turbulent orographic form drag (Gu et al., 2023). As shown in Figure 7, the WRF_CFSv2 consistently overestimates the zonal wind (U) throughout a day (Fig. 7a), whereas the meridional wind (V) remains comparable to the ERA5 (Fig. 7b). The positive biases of the predicted U component are primarily attributed to the overestimated geostrophic wind component (Fig. 7a). The WRF_CFSv2 can reproduce the diurnal cycle of the ageostrophic wind in the ERA5, suggesting that the WRF_CFSv2 can effectively capture the inertial oscillations. It is worth noting that the ERA5 data exhibits two sharp changes at 05:00–06:00 and 17:00–18:00 BJT, respectively; these are known artifacts caused by the data assimilation method reported in previous studies (Chen et al., 2021). Previous comparisons with independent observations and other reanalysis datasets have demonstrated that ERA5 can reliably reproduce the overall diurnal evolution of regional winds (Cui et al., 2023; Wu et al., 2026). Moreover, the present conclusions are based on the coherent, multi-hour nocturnal enhancement of ageostrophic winds and moisture convergence rather than on isolated values at the assimilation-transition hours. Therefore, although these discontinuities may affect the exact amplitudes at individual hours, they are unlikely to alter the main physical interpretation or the overall conclusions. However, regarding the U component, the WRF_CFSv2 overestimates the amplitude of the ageostrophic wind, which further intensifies the zonal wind speed in the early morning. Additionally,

In Press
For Review Only

423 the predicted V component peaks earlier than observation, which is corresponding to
424 the slight temporal advance of the early-morning precipitation peak in the WRF_CFSv2.



425

426 **Fig. 6.** The mean 850 hPa wind vectors and wind speed (shadings) during the RPEs at
427 0200 BJT, 0800 BJT, 1400 BJT, and 2000 BJT from ERA5 (a-d), WRF_CFSv2
428 predictions (e-h) and the difference between the WRF_CFSv2 and ERA5 (i-l) in the
429 summers of 2020-2024.

In Press

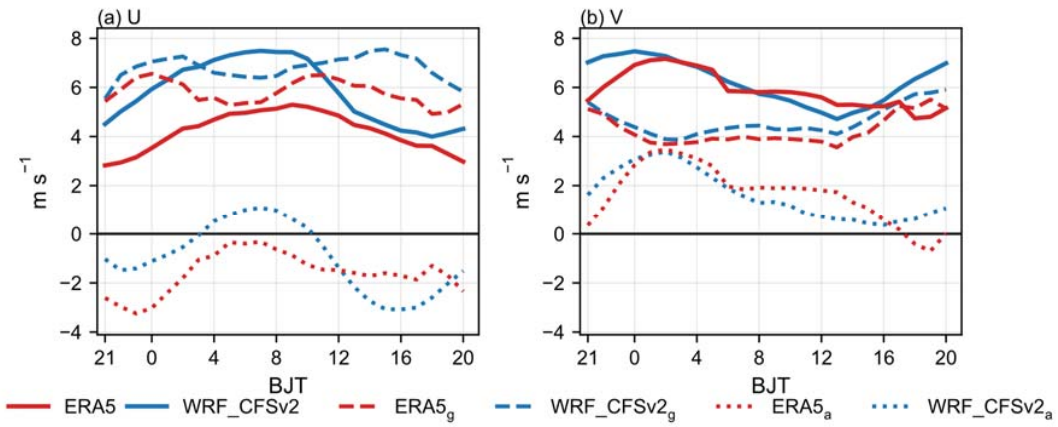
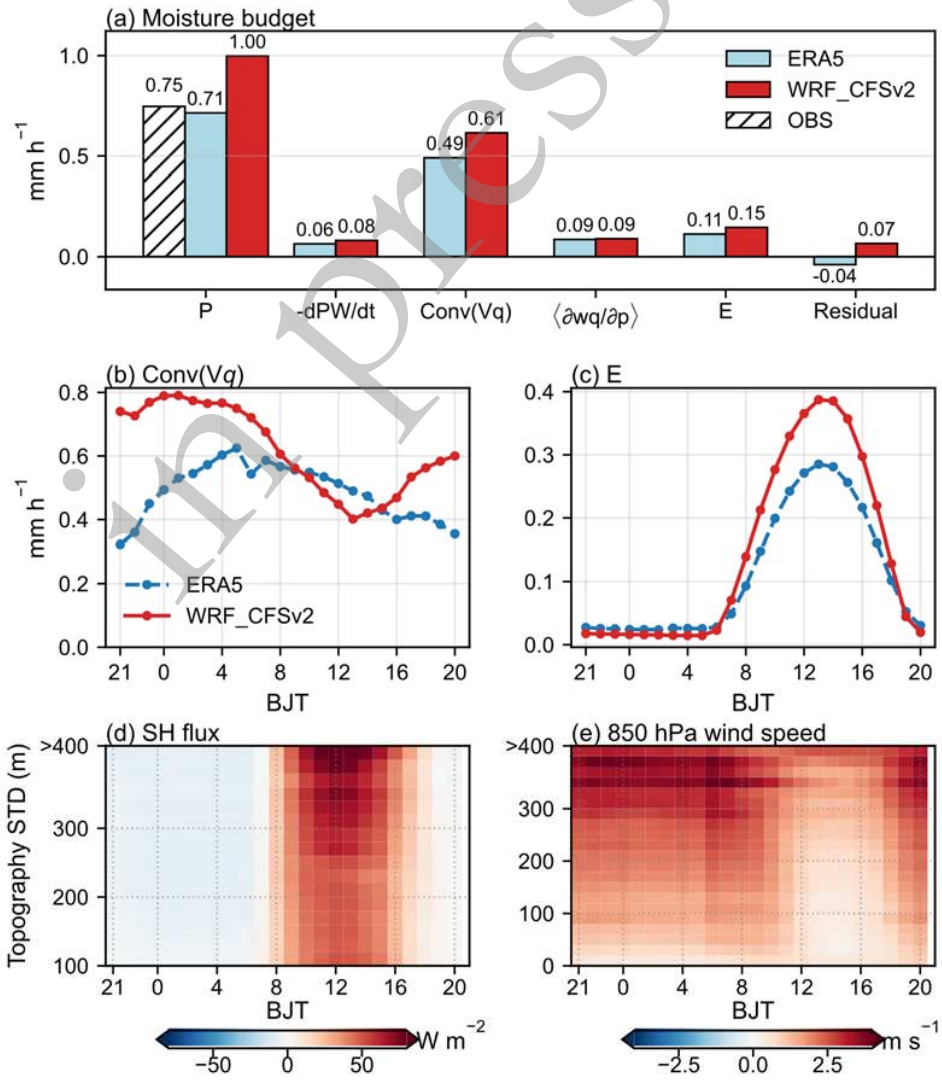


Fig. 7. Diurnal variations of (a) zonal (U) and (b) meridional (V) winds, including their geostrophic and ageostrophic components regionally averaged over the region bounded by 107°E–120°E and 23°N–28°N during the RPEs in the summers of 2020-2024 from the ERA5 and WRF_CFSv2 predictions.

To investigate the moisture supply during RPEs, we conducted a moisture budget analysis (Fig. 8a), with evaporation in the WRF_CFSv2 estimated from the surface latent heat flux. Observed precipitation was included as an independent reference to assess the reliability of ERA5 precipitation. The ERA5 precipitation rate (0.71 mm h^{-1}) agrees closely with the observed value (0.75 mm h^{-1}), supporting its reliability. In contrast, the WRF_CFSv2 produces a precipitation rate of 1.00 mm h^{-1}, approximately 40% higher than ERA5 and 33% higher than the observations. In the ERA5 reanalysis, the WVFC into the MLYRB is 0.49 mm h^{-1}, significantly exceeding the evaporation term (0.11 mm h^{-1}), indicating that RPEs in this region are dominated by large-scale convergence. In the WRF_CFSv2, large-scale convergence remains the largest contributor (0.61 mm h^{-1}) and is the primary source of error with the deviations of 0.12 mm h^{-1} relative to the ERA5. The evaporation overestimated by 0.04 mm h^{-1} is the

For Review Only
in Press

447 second-largest component, whereas the vertical-transport and local-storage terms are
448 comparatively lower. Therefore, the diurnal variations in these two minor terms are not
449 discussed further. Overall, the overestimation of RPE precipitation predicted by the
450 WRF_CFSv2 is primarily attributable to excessive dynamical moisture convergence.
451 The residual may reflect systematic differences between the ERA5 and WRF_CFSv2
452 data systems, as well as incomplete closure arising from the offline pressure-level
453 diagnosis. The omission of condensate tendency terms may also contribute; therefore,
454 the residual is retained explicitly but is not attributed to a specific physical process.



455

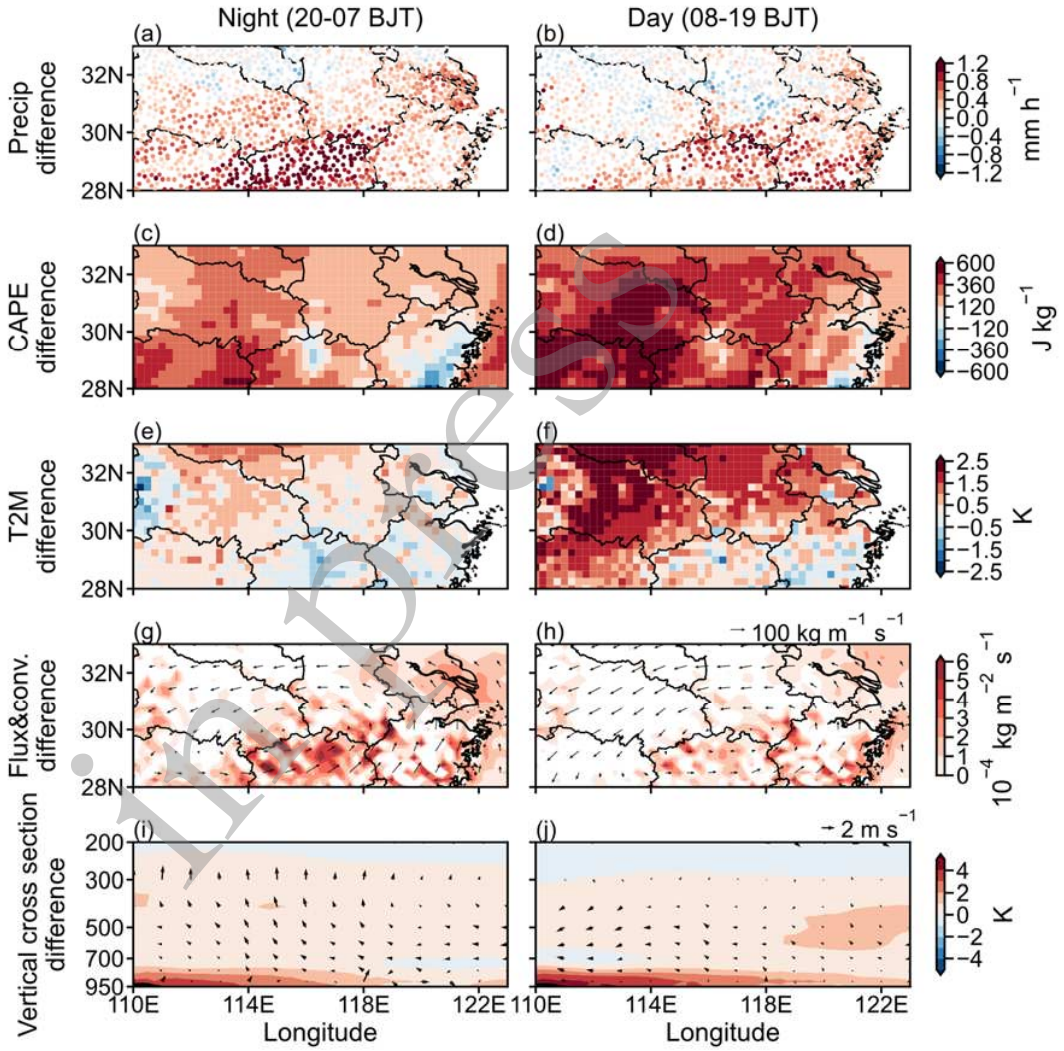
Fig. 8. Comparison of moisture budget components from ERA5 and WRF_CFSv2 predictions regionally averaged over the MLYRB during the RPEs in summers of 2020-2024, for the precipitation component, the observations are included for comparison with ERA5 and WRF_CFSv2 (a). The diurnal variations of the 2 components in **a** are shown in **b-c**. The mean prediction biases of the predicted sensible heat flux (850 hPa wind speed) during the RPEs regionally averaged over the grids with different STDs in the MLYRB (the region of 110°E–123°E, 23°N–33°N) (d-e).

To further investigate the sources of the prediction bias of regional precipitation amount, we separately analyzed the driving factors during the daytime and nighttime. At night, the overestimated precipitation is centered over northern Jiangxi Province and the Huangshan Mountains (Fig. 9a). The WRF_CFSv2 produces a persistent anomalous low-level cyclonic circulation, with excessively strong southwesterly flow over and to the south of the MLYRB (Figs. 6i, j). This anomalous flow strengthens northward moisture transport and produces excessive WVFC over most of the basin (Fig. 9g). The WVFC bias spatially overlaps the positive precipitation bias and coincides with overly strong low-level convergence and large-scale ascent (Figs. 9a, g, i and 10g). These dynamical biases are also coherent in time, showing pronounced nocturnal and early-morning enhancement. By contrast, the CAPE and 2-m air temperature biases are much weaker during nighttime than during daytime (Figs. 9c, e), indicating a limited thermodynamic contribution. The moisture-budget analysis further indicates that WVFC exhibits the largest positive bias among the diagnosed moisture-source terms (Fig. 8a). The circulation, moisture-convergence, and precipitation biases show broadly

For Review Only
In Press

478 consistent spatial and temporal variations, suggesting a link between the overly strong
479 nocturnal synoptic circulation and the overestimation of nighttime and early-morning
480 precipitation.

481



482

483 **Fig. 9.** Spatial distribution of the differences of precipitation (a, b), CAPE (c, d), 2m air
484 temperature (e, f), the vertically integrated (from surface to 100 hPa) water vapour
485 transport flux and its convergence (g, h), the pressure - longitude cross sections of
486 equivalent potential temperature (shaded) and atmospheric circulation (vector; vertical

487 velocity is magnified by 100) averaged along 28–33°N (i, j) during the RPEs in
488 summers of 2020-2024 between the WRF_CFSv2 predictions and observations/ERA5
489 for nighttime and daytime.

490 Figure 10 further illustrates the diurnal evolution of the vertical atmospheric
491 structure during RPEs over the MLYRB. At all three times, the convergence zone tilts
492 northward with height, exhibiting a typical vertical configuration characterized by low-
493 level convergence, upper-level divergence, and strong ascent in the middle troposphere
494 (Figs. 10a-c). In the ERA5, both the ascending motion and low-level convergence reach
495 their maximum intensity and deepest vertical extent at approximately 10:00 BJT (Fig.
496 10b), after which they gradually weaken. By contrast, WRF_CFSv2 exhibits a weaker
497 diurnal variation, with the strongest circulation occurring prematurely at 02:00 BJT (Fig.
498 10d). The difference fields further show that the overestimations of ascending motion,
499 low-level convergence, and upper-level divergence all peak at 02:00 BJT (Fig. 10g).
500 These results provide additional dynamical evidence that WRF_CFSv2 produces an
501 excessively strong nocturnal large-scale circulation associated with the Meiyu frontal
502 system. The enhanced low-level convergence and upward moisture transport,
503 accompanied by intensified WVFC, contribute to the overestimation of nocturnal
504 precipitation.

For Review Only
in Press

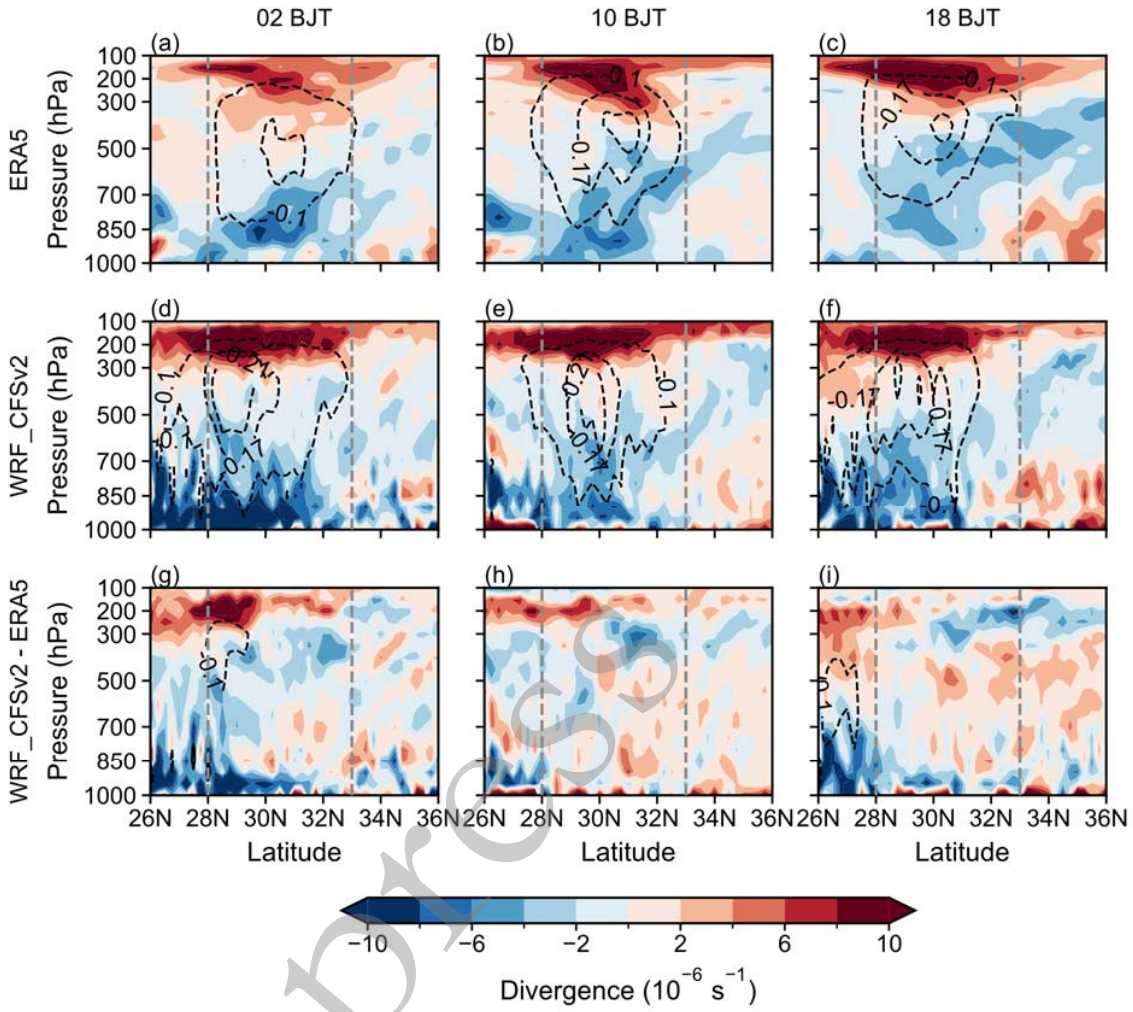


Fig. 10. Pressure-latitude cross sections of divergence (shading) and pressure vertical velocity (black contours; Pa s^{-1}), averaged along 110°–122°E at 02:00, 10:00, and 18:00 BJT (from left to right) during the RPEs from ERA5 (a-c) and WRF_CFSv2 (d-f), and the differences between the WRF_CFSv2 and ERA5 (g–i). Gray dashed lines mark 28°N and 33°N.

During the daytime, significant precipitation overestimation shift to areas with complex terrain, including the Huangshan Mountains, the Mufu Mountains, southern Zhejiang Province, and the western mountainous regions of Hubei (Fig. 9b). the WRF_CFSv2 tends to overestimate surface latent and sensible heat fluxes compared to

in press only

the ERA5 (not shown). Notably, in regions where the STD exceeds 100 m, the overestimation of daytime sensible heat flux intensifies with terrain complexity (Fig. 8d), indicating a need to improve the surface thermal process parameterizations over complex topography. This amplified surface heating substantially elevates the low-level equivalent potential temperature (Fig. 9j) and 2m temperature (Fig. 9f), generating greater CAPE (Fig. 9d). This daytime thermodynamic enhancement combines with the pre-existing, over-predicted daytime WVFC (Fig. 9h), leading to the overestimation of daytime precipitation. In summary, while daytime precipitation overestimation is fundamentally sustained by excessive moisture convergence and evaporation, the thermodynamic instability triggered by exaggerated surface heating acts as an amplifying factor that exacerbates the rainfall.

4. Summary and Discussion

In this study, we used the rain gauge observations and ERA5 reanalysis data to evaluate the ability of the WRF_CFSv2 to predict the diurnal cycle of RPEs over the MLYRB in summer. Meanwhile, the possible causes related to the model biases are also explored. The main conclusions are summarized as follows:

The WRF_CFSv2 can well reproduce the spatial distribution of the climatic mean precipitation amount and frequency over the MLYRB in summer despite the overestimation of their magnitudes. While the WRF_CFSv2 well predicts the magnitude of precipitation intensity, it shows relatively lower skill in reproducing its spatial distribution relative to the precipitation amount and frequency. Further analysis

For Review Only
in Press

indicated that the overestimated RPEs largely contribute to the overestimation of total precipitation relative to the LPEs.

Additionally, the WRF_CFSv2 can generally reproduce the 3 diurnal cycle types of RPEs. However, the second type (daytime-dominant) and the third type (bimodal morning-afternoon peak) predicted by the WRF_CFSv2 are located slightly farther southeastward relative to the observation. The WRF_CFSv2 can also well reproduce the diurnal phase of the observed RPEs despite clear biases: it overestimates the precipitation amount of RPEs at all hours of a day with the morning peak occurring one hour earlier than the observation; and this overestimated precipitation amount is primarily attributed to the overestimation of the precipitation coverage rate throughout a day, and is further amplified by the overestimated precipitation intensity during the afternoon and nighttime.

Further analysis of possible causes related to these biases mentioned above indicates that the overestimated precipitation amount of RPEs over the MLYRB is dominated by the dynamic factors, while the thermodynamic factors play a secondary role. Dynamically, the WRF_CFSv2 produces a persistent anomalous low-level cyclonic system over the region, which leads to an overestimation of low-level southwesterly winds. Coupled with the uplift induced by large-scale synoptic systems, this anomalous system enhances WVFC, which results in the overestimation of nocturnal RPEs. Thermodynamically, a near-surface warm bias leads to an excessive atmospheric instability. This heightened instability, combined with excessive evaporation and strong WVFC, ultimately culminates in the overestimation of daytime

For Review Only
in Press

RPEs.

It should be noted that this study evaluates the WRF_CFSv2 in its established operational configuration, which uses a 9-km grid spacing, the GF cumulus parameterization, and the WSM3 microphysics scheme. The 9-km grid lies within the convective "gray zone," where interactions between explicitly resolved and parameterized convection may introduce errors in convective initiation, low-level winds, and moisture convergence, potentially contributing to the overestimation of RPEs (Ou et al., 2020). In addition, WSM3 combines cloud water/ice and rain/snow and lacks separate supercooled-liquid-water and graupel categories (Hong et al., 2004). Its simplified mixed-phase treatment may alter latent heating and cooling, hydrometeor loading and sedimentation, and cold-pool evolution, thereby affecting convective organization, lifetime, precipitation efficiency, and moisture depletion (Cossu and Hocke, 2014; Wu et al., 2023). Because the objective is to assess the actual performance of the operational system, its existing configuration was retained. Future upgrades will evaluate finer convection-permitting grids and more comprehensive mixed-phase microphysics schemes.

Another caveat is that this study uses forecasts at lead times of 13–36 h from the daily 00:00 UTC initializations, so different BJT hours correspond to different forecast lead times. The diagnosed diurnal biases may therefore also contain error signals that evolve with forecast lead time, especially at the transition where the 36-h forecast from one cycle is replaced by the 13-h forecast from the next. Future work could use forecasts for the same valid time from different initialization cycles and lead times to further

In Press For Review Only

separate diurnal biases from their lead-time dependence. For operational forecasting, statistical post-processing relationships conditioned on forecast lead time and local time could also be developed. Bias-correction methods such as frequency matching, quantile mapping, or model output statistics could then be applied to reduce systematic biases in precipitation frequency and intensity, thereby further improving forecast skill for RPEs (Zhu and Luo, 2015; Vannitsem et al., 2021).

Overall, the prediction biases of RPEs are mainly related to inadequate prediction of the local thermal processes and large-scale low-level wind fields. Previous studies have shown that including the sub-grid terrain solar radiative effect (Huang et al., 2022; Cai et al., 2023) can effectively improve the simulation of surface thermal conditions over complex terrain, and including the sub-grid turbulent orographic form drag (Gu et al., 2023; Zhou et al., 2024) can alleviate the overestimation of low-level wind speeds caused by neglecting sub-grid topographic turbulent drag. Therefore, to further improve the ability of the WRF_CFSv2 to predict the RPEs, the sub-grid terrain radiative and dynamic effects will be included in the WRF_CFSv2 in the near future.

Acknowledgments. This study is supported by the National Natural Science Foundation of China under Grant U2342207 and the Jiangsu Collaborative Innovation Center for Climate Change. We appreciate the High Performance Computing Center of Nanjing University.

REFERENCES

In Press
For Review Only

Cai, S., A. Huang, K. Zhu, W. Guo, Y. Wu, and C. Gu, 2023: The Forecast Skill of the Summer Precipitation Over Tibetan Plateau Improved by the Adoption of a 3D Sub-Grid Terrain Solar Radiative Effect Scheme in a Convection-Permitting Model. *Journal of Geophysical Research: Atmospheres*, **128**, e2022JD038105, https://doi.org/10.1029/2022JD038105.

Cai, S., A. Huang, K. Zhu, B. Yang, X. Yang, Y. Wu, and X. Mu, 2021: Diurnal cycle of summer precipitation over the Eastern Tibetan Plateau and surrounding regions simulated in a convection-permitting model. *Climate Dynamics*, **57**, 611–632, https://doi.org/10.1007/s00382-021-05729-5.

Chen, F., and J. Dudhia, 2001: Coupling an Advanced Land Surface–Hydrology Model with the Penn State–NCAR MM5 Modeling System. Part I: Model Implementation and Sensitivity. *Monthly Weather Review*, **129**, 569–585, https://doi.org/10.1175/1520-0493(2001)129<0569:CAALSH>2.0.CO;2.

Chen, G., W. Sha, and T. Iwasaki, 2009: Diurnal variation of precipitation over southeastern China: Spatial distribution and its seasonality. *Journal of Geophysical Research: Atmospheres*, **114**, https://doi.org/10.1029/2008JD011103.

Chen, G., Y. Du, and Z. Wen, 2021: Seasonal, Interannual, and Interdecadal Variations of the East Asian Summer Monsoon: A Diurnal-Cycle Perspective. *Journal of Climate*, **34**, 4403–4421, https://doi.org/10.1175/JCLI-D-20-0882.1.

Chen, G., W. Sha, T. Iwasaki, and K. Ueno, 2012: Diurnal variation of rainfall in the Yangtze River Valley during the spring-summer transition from TRMM measurements. *Journal of Geophysical Research: Atmospheres*, **117**, https://doi.org/10.1029/2011JD017056.

Chen, G., W. Sha, M. Sawada, and T. Iwasaki, 2013: Influence of summer monsoon diurnal cycle on moisture transport and precipitation over eastern China. *Journal of Geophysical Research:*

In Press For Review Only

Atmospheres, **118**, 3163–3177, https://doi.org/10.1002/jgrd.50337.

Chen, S., B. Yang, A. Huang, and Y. Zhang, 2025: Terrain and urban impacts on summer extreme precipitation over Henan, China: A synoptic and simulation analysis. *Atmospheric Research*, **320**, 108033, https://doi.org/10.1016/j.atmosres.2025.108033.

Chou, C., and C.-W. Lan, 2012: Changes in the Annual Range of Precipitation under Global Warming. *Journal of Climate*, **25**, 222–235, https://doi.org/10.1175/JCLI-D-11-00097.1.

Cossu, F., and K. Hocke, 2014: Influence of microphysical schemes on atmospheric water in the Weather Research and Forecasting model. *Geosci. Model Dev.*, **7**, 147–160, https://doi.org/10.5194/gmd-7-147-2014.

Cui, C., and Coauthors, 2023: Analysis of the Characteristics of the Low-level Jets in the Middle Reaches of the Yangtze River during the Mei-yu Season. *Advances in Atmospheric Sciences*, **40**, 711–724, https://doi.org/10.1007/s00376-022-2107-1.

Dai, A., 2006: Precipitation Characteristics in Eighteen Coupled Climate Models. *Journal of Climate*, **19**, 4605–4630, https://doi.org/10.1175/JCLI3884.1.

Dai, A., and K. E. Trenberth, 2004: The Diurnal Cycle and Its Depiction in the Community Climate System Model. *Journal of Climate*, **17**, 930–951, https://doi.org/10.1175/1520-0442(2004)017<0930:TDCAID>2.0.CO;2.

Dai, A., F. Giorgi, and K. E. Trenberth, 1999: Observed and model-simulated diurnal cycles of precipitation over the contiguous United States. *Journal of Geophysical Research: Atmospheres*, **104**, 6377–6402, https://doi.org/10.1029/98JD02720.

Dong, G., Z. Jiang, Y. Wang, Z. Tian, and J. Liu, 2022: Evaluation of extreme precipitation in the Yangtze River Delta Region of China using a 1.5 km mesh convection-permitting regional

For Review Only
In Press

climate model. *Climate Dynamics*, **59**, 2257–2273, https://doi.org/10.1007/s00382-022-06208-1.

Fu, P., K. Zhu, K. Zhao, B. Zhou, and M. Xue, 2019: Role of the Nocturnal Low-level Jet in the Formation of the Morning Precipitation Peak over the Dabie Mountains. *Advances in Atmospheric Sciences*, **36**, 15–28, https://doi.org/10.1007/s00376-018-8095-5.

GEBCO Bathymetric Compilation Group 2025 ,2025: The GEBCO_2025 Grid - a continuous terrain model for oceans and land at 15 arc-second intervals. NERC EDS British Oceanographic Data Centre NOC, https://doi.org/10.5285/37c52e96-24ea-67ce-e063-7086abc05f29.

Grell, G. A., and S. R. Freitas, 2014: A scale and aerosol aware stochastic convective parameterization for weather and air quality modeling. *Atmos. Chem. Phys.*, **14**, 5233–5250, https://doi.org/10.5194/acp-14-5233-2014.

Gu, C., A. Huang, X. Li, B. Yang, X. Zhou, and Y. Wu, 2023: Impact of Sub-Grid Turbulent Orographic Form Drag on the Summer Monsoon Precipitation Simulation Over China. *Journal of Geophysical Research: Atmospheres*, **128**, e2023JD039113, https://doi.org/10.1029/2023JD039113.

Guo, J., and Coauthors, 2017: Declining frequency of summertime local-scale precipitation over eastern China from 1970 to 2010 and its potential link to aerosols. *Geophysical Research Letters*, **44**, 5700–5708, https://doi.org/10.1002/2017GL073533.

Guo, Z., J. Fang, X. Sun, J. Tang, Y. Yang, and J. Tang, 2020: Decadal long convection-permitting regional climate simulations over eastern China: evaluation of diurnal cycle of precipitation. *Climate Dynamics*, **54**, 1329–1349, https://doi.org/10.1007/s00382-019-05061-z.

Hersbach, H., and Coauthors, 2020: The ERA5 global reanalysis. *Quarterly Journal of the Royal Meteorological Society*, **146**, 1999–2049, https://doi.org/10.1002/qj.3803.

In Press
For Review Only

667 Hong, S.-Y., J. Dudhia, and S.-H. Chen, 2004: A Revised Approach to Ice Microphysical Processes
668 for the Bulk Parameterization of Clouds and Precipitation. *Monthly Weather Review*, **132**, 103–
669 120, https://doi.org/10.1175/1520-0493(2004)132<0103:ARATIM>2.0.CO;2.
670 Hong, S.-Y., Y. Noh, and J. Dudhia, 2006: A New Vertical Diffusion Package with an Explicit
671 Treatment of Entrainment Processes. *Monthly Weather Review*, **134**, 2318–2341,
672 https://doi.org/10.1175/MWR3199.1.
673 Hu, X., and W. Yuan, 2021: Evaluation of ERA5 precipitation over the eastern periphery of the
674 Tibetan plateau from the perspective of regional rainfall events. *International Journal of*
675 *Climatology*, **41**, 2625–2637, https://doi.org/10.1002/joc.6980.
676 Hu, Y., Y. Deng, Z. Zhou, C. Cui, and X. Dong, 2019: A statistical and dynamical characterization
677 of large-scale circulation patterns associated with summer extreme precipitation over the middle
678 reaches of Yangtze river. *Climate Dynamics*, **52**, 6213–6228, https://doi.org/10.1007/s00382-018-
679 4501-z.
680 Huang, A., and Coauthors, 2022: Development of a Clear-Sky 3D Sub-Grid Terrain Solar Radiative
681 Effect Parameterization Scheme Based on the Mountain Radiation Theory. *Journal of*
682 *Geophysical Research: Atmospheres*, **127**, e2022JD036449,
683 https://doi.org/10.1029/2022JD036449.
684 Iacono, M. J., J. S. Delamere, E. J. Mlawer, M. W. Shephard, S. A. Clough, and W. D. Collins, 2008:
685 Radiative forcing by long-lived greenhouse gases: Calculations with the AER radiative transfer
686 models. *Journal of Geophysical Research: Atmospheres*, **113**,
687 https://doi.org/10.1029/2008JD009944.
688 Lai, H.-W., T. Ou, A. Dai, X. Chen, and A. Chen, 2025: Diurnal Cycle of Summer Precipitation

For Review Only
In Press

Over Mainland Southeast Asia Revealed by Observations, Reanalysis, and Dynamic Downscaling. *Journal of Geophysical Research: Atmospheres*, **130**, e2024JD043020, https://doi.org/10.1029/2024JD043020.

Li, J., 2018: Hourly station-based precipitation characteristics over the Tibetan Plateau. *International Journal of Climatology*, **38**, 1560–1570, https://doi.org/10.1002/joc.5281.

Li, L., J. Li, and R. Yu, 2020a: Characteristics of summer regional rainfall events over Ili River Valley in Northwest China. *Atmospheric Research*, **243**, 104996, https://doi.org/10.1016/j.atmosres.2020.104996.

Li, P., K. Furtado, T. Zhou, H. Chen, J. Li, Z. Guo, and C. Xiao, 2020b: The diurnal cycle of East Asian summer monsoon precipitation simulated by the Met Office Unified Model at convection-permitting scales. *Climate Dynamics*, **55**, 131–151, https://doi.org/10.1007/s00382-018-4368-z.

Liu, J., L. Yang, J. Jiang, W. Yuan, and Z. Duan, 2021: Mapping diurnal cycles of precipitation over China through clustering. *Journal of Hydrology*, **592**, 125804, https://doi.org/10.1016/j.jhydrol.2020.125804.

Ou, T., D. Chen, X. Chen, C. Lin, K. Yang, H.-W. Lai, and F. Zhang, 2020: Simulation of summer precipitation diurnal cycles over the Tibetan Plateau at the gray-zone grid spacing for cumulus parameterization. *Climate Dynamics*, **54**, 3525–3539, https://doi.org/10.1007/s00382-020-05181-x.

Qiao, F., and X.-Z. Liang, 2016: Effects of cumulus parameterization closures on simulations of summer precipitation over the United States coastal oceans. *Journal of Advances in Modeling Earth Systems*, **8**, 764–785, https://doi.org/10.1002/2015MS000621.

Robertson, A. W., N. Vigaud, J. Yuan, and M. K. Tippett, 2020: Toward Identifying Subseasonal

In Press For Review Only

Forecasts of Opportunity Using North American Weather Regimes. *Monthly Weather Review*, **148**, 1861–1875, https://doi.org/10.1175/mwr-d-19-0285.1.

Saha, S., and Coauthors, 2014: The NCEP Climate Forecast System Version 2. *Journal of Climate*, **27**, 2185–2208, https://doi.org/10.1175/JCLI-D-12-00823.1.

Seager, R., N. Naik, and G. A. Vecchi, 2010: Thermodynamic and Dynamic Mechanisms for Large-Scale Changes in the Hydrological Cycle in Response to Global Warming. *Journal of Climate*, **23**, 4651–4668, https://doi.org/10.1175/2010JCLI3655.1.

Skamarock, W. C., and Coauthors, 2008: A Description of the Advanced Research WRF Version 3. NCAR Technical Note NCAR/TN-475+STR June 2008 Mesoscale and Microscale Meteorology Division National Center for Atmospheric Research Boulder **475**, 1, https://doi.org/10.5065/D68S4MVH.

Sorooshian, S., X. Gao, K. Hsu, R. A. Maddox, Y. Hong, H. V. Gupta, and B. Imam, 2002: Diurnal Variability of Tropical Rainfall Retrieved from Combined GOES and TRMM Satellite Information. *Journal of Climate*, **15**, 983–1001, https://doi.org/10.1175/1520-0442(2002)015<0983:DVOTRR>2.0.CO;2.

Tang, Y., A. Huang, P. Wu, D. Huang, D. Xue, and Y. Wu, 2021: Drivers of Summer Extreme Precipitation Events Over East China. *Geophysical Research Letters*, **48**, e2021GL093670, https://doi.org/10.1029/2021GL093670.

Vannitsem, S., and Coauthors, 2021: Statistical Postprocessing for Weather Forecasts: Review, Challenges, and Avenues in a Big Data World. *Bulletin of the American Meteorological Society*, **102**, E681–E699, https://doi.org/10.1175/BAMS-D-19-0308.1.

Vigaud, N., A. W. Robertson, and M. K. Tippett, 2018: Predictability of Recurrent Weather Regimes

In Press
For Review Only

over North America during Winter from Submonthly Reforecasts. *Monthly Weather Review*, **146**, 2559–2577, https://doi.org/10.1175/mwr-d-18-0058.1.

Wei, Q., J. Sun, S. Fu, Y. Zhang, and X. Wang, 2024: Spatiotemporal Characteristics of Rainfall over Different Terrain Features in the Middle Reaches of the Yangtze River Basin during the Warm Seasons of 2016–20. *Advances in Atmospheric Sciences*, **41**, 915–936, https://doi.org/10.1007/s00376-023-3034-5.

Wu, D., L. Ma, T. Hu, and R. Zhang, 2023: Impacts of microphysical parameterizations on banded convective system in convection-permitting simulation: a case study. *Frontiers in Earth Science*, **Volume 11 - 2023**, https://doi.org/10.3389/feart.2023.1149518.

Wu, R., A. Huang, D. Huang, J. Tang, and X. Xu, 2025: Characteristics of the Summer Regional Precipitation Events in the Middle and Lower Yangtze River Basin and Associated Mechanisms. *Journal of Geophysical Research: Atmospheres*, **130**, e2024JD042622, https://doi.org/10.1029/2024JD042622.

Wu, R., A. Huang, D. Huang, C. Gu, and S. Li, 2026: Regulatory Factors of the Morning Peak of Summer Regional Precipitation Events Over the Middle and Lower Yangtze River Basin, China. *Geophysical Research Letters*, **53**, e2026GL123617, https://doi.org/10.1029/2026GL123617.

Wu, Y., and Coauthors, 2018: Diurnal variations of summer precipitation over the regions east to Tibetan Plateau. *Climate Dynamics*, **51**, 4287–4307, https://doi.org/10.1007/s00382-017-4042-x.

Xu, M., and Coauthors, 2021: Convection-Permitting Hindcasting of Diurnal Variation of Mei-yu Rainfall Over East China With a Global Variable-Resolution Model. *Journal of Geophysical Research: Atmospheres*, **126**, e2021JD034823, https://doi.org/10.1029/2021JD034823.

Xue, M., X. Luo, K. Zhu, Z. Sun, and J. Fei, 2018: The Controlling Role of Boundary Layer Inertial

In Press
For Review Only

Oscillations in Meiyu Frontal Precipitation and Its Diurnal Cycles Over China. *Journal of Geophysical Research: Atmospheres*, **123**, 5090–5115, https://doi.org/10.1029/2018JD028368.

Yang, B., Y. Zhou, Y. Zhang, A. Huang, Y. Qian, and L. Zhang, 2018: Simulated precipitation diurnal cycles over East Asia using different CAPE-based convective closure schemes in WRF model. *Climate Dynamics*, **50**, 1639–1658, https://doi.org/10.1007/s00382-017-3712-z.

Yu, R., Y. Xu, T. Zhou, and J. Li, 2007a: Relation between rainfall duration and diurnal variation in the warm season precipitation over central eastern China. *Geophysical Research Letters*, **34**, https://doi.org/10.1029/2007GL030315.

Yu, R., T. Zhou, A. Xiong, Y. Zhu, and J. Li, 2007b: Diurnal variations of summer precipitation over contiguous China. *Geophysical Research Letters*, **34**, https://doi.org/10.1029/2006GL028129.

Zeng, J., and Coauthors, 2023: Typical Synoptic Patterns Responsible for Summer Regional Hourly Extreme Precipitation Events Over the Middle and Lower Yangtze River Basin, China. *Geophysical Research Letters*, **50**, e2023GL104829, https://doi.org/10.1029/2023GL104829.

Zhang, Q., Zhao, Y., Fan, S. 2016: Development of hourly precipitation datasets for national meteorological stations in China. Torrential Rain Disasters, **35**, 182–186, https://doi.org/10.3969/j.issn.1004-9045.2016.02.011. (in Chinese)

Zhang, Y., M. Xue, K. Zhu, and B. Zhou, 2019: What Is the Main Cause of Diurnal Variation and Nocturnal Peak of Summer Precipitation in Sichuan Basin, China? The Key Role of Boundary Layer Low-Level Jet Inertial Oscillations. *Journal of Geophysical Research: Atmospheres*, **124**, 2643–2664, https://doi.org/10.1029/2018JD029834.

Zhao, Y., X. Peng, X. Li, and S. Chen, 2024: Improved Diurnal Cycle of Precipitation on Land in a Global Non-Hydrostatic Model Using a Revised NSAS Deep Convective Scheme. *Advances in*

For Review Only
In Press

Atmospheric Sciences, **41**, 1217–1234, https://doi.org/10.1007/s00376-023-3121-7.

Zhou, T., R. Yu, H. Chen, A. Dai, and Y. Pan, 2008: Summer Precipitation Frequency, Intensity, and Diurnal Cycle over China: A Comparison of Satellite Data with Rain Gauge Observations. *Journal of Climate*, **21**, 3997–4010, https://doi.org/10.1175/2008JCLI2028.1.

Zhou, Y., A. Huang, X. Li, C. Gu, and Y. Wu, 2024: Local and Remote Effects of the Sub-Grid Turbulent Orographic Form Drag on the Summer Monsoon Precipitation Over Eastern China. *Journal of Geophysical Research: Atmospheres*, **129**, e2024JD041173, https://doi.org/10.1029/2024JD041173.

Zhu, L., J. Liu, A.-X. Zhu, M. Sheng, and Z. Duan, 2018: Spatial Distribution of Diurnal Rainfall Variation in Summer over China. *Journal of Hydrometeorology*, **19**, 667–678, https://doi.org/10.1175/JHM-D-17-0176.1.

Zhu, Y., and Y. Luo, 2015: Precipitation Calibration Based on the Frequency-Matching Method. *Weather and Forecasting*, **30**, 1109–1124, https://doi.org/10.1175/WAF-D-13-00049.1.

For Review Only

in Press